ACS NANO

www.acsnano.org

Article

A Self-Driving and Self-Reporting Petal-Like Au−Cu_2O Metalloenzyme for Probing H_2S-Mediated Cuproptosis

Lei Jiang, Qiaoyi Lu, Ermeng Gong, Jiwei Liu, Hongliu Yu, Boyu Ren, Lingniu Yang, Siqi He, and Youju Huang*

Cite This: *ACS Nano* 2026, 20, 10151−10162

Read Online

ACCESS | Metrics & More | Article Recommendations | Supporting Information

ABSTRACT: Hydrogen sulfide (H_2S), highly enriched in colorectal tumors, acts as an upstream regulator of copper homeostasis and cuproptosis. However, most existing cuproptosis nanotherapeutics focus on downstream copper overload while lacking the ability to resolve the dynamic H_2S-mediated regulation that governs copper speciation and redox stress. Here, we develop a self-driving and self-reporting petal-like Au−Cu_2O metalloenzyme that enables real-time interrogation of H_2S-mediated cuproptosis. Surfactant-directed anisotropic growth yields an interface-rich architecture with exposed Au−Cu_2O junctions, generating abundant plasmonic hotspots and redox-active sites for synergistic SERS enhancement and photoenhanced peroxidase-like catalysis. The nanocomposite drives sustained Cu^+/Cu^{2+} cycling, glutathione depletion, and reactive oxygen species generation, leading to mitochondrial dysfunction and lipid peroxidation. Using activity-based SERS monitoring in living cells, we reveal that H_2S exerts a dual regulatory role by transiently buffering oxidative stress while promoting intracellular copper retention through copper-sulfide complexation, thereby amplifying downstream cuproptosis execution. By correlating H_2S upregulation with copper retention and cuproptosis markers in colorectal cancer models, this work establishes a foundation for precision intervention against H_2S-altered malignancies.

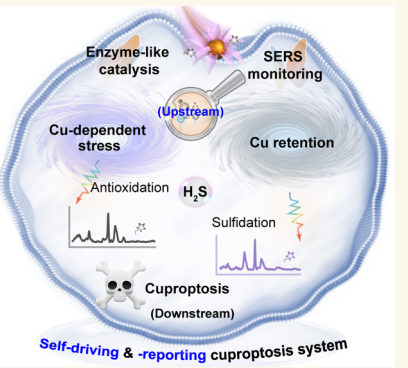

KEYWORDS: *cuproptosis, theranostic nanoplatforms, H_2S regulation, Au−Cu_2O heterostructures, activity-based SERS*

Cuproptosis, a recently identified form of Cu-dependent programmed cell death, presents new therapeutic opportunities for regulating Cu levels in targeting metabolically active cancers, particularly those resistant to conventional treatments.[1−3] Although not primarily mediated by oxidative stress, cuproptosis is associated with a significant increase of reactive oxygen species (ROS) generation due to the high Cu-mediated Fenton catalytic efficiency (Cu^{2+}: 460 $M^{-1}{\cdot}s^{-1}$, Cu^+: 10000 $M^{-1}{\cdot}s^{-1}$), which exacerbates mitochondrial damage and disrupts redox dysregulation.[4−6] Cuproptosis inducers typically exploit specific features of tumor microenvironment (TME), such as enriched GSH, elevated level of H_2O_2, and mild acidity.[7−9] In colorectal cancer (CRC), the TME is uniquely characterized by elevated high levels of hydrogen sulfide (H_2S).[10−12] It can interact with copper ions to form copper-sulfide complexes, potentially creating a bioavailable copper reservoir that modulates copper bioavailability and redox activity.[13,14] This positions H_2S metabolism as a crucial upstream regulator of copper homeostasis, yet the dynamic relationship between upstream H_2S fluctuations and downstream copper-induced redox dysregulation remains poorly understood, limiting the development of precise cuproptosis-based therapies.

Recent years have witnessed growing interest in leveraging H_2S as a trigger for CRC-targeting theranostic agents. Various H_2S-responsive systems, including BODIPY probes, Cu-MOFs, and copper single-atom nanozymes, have been developed for photothermal and photodynamic therapy.[14−16] For instance, Zhao et al. developed copper-ion-interference therapy using H_2S-responsive copper hydroxyphosphate nanoparticles to disrupt copper homeostasis.[4] Despite their therapeutic promise, these approaches predominantly focus on downstream copper overload and therapeutic efficacy, while functioning as "blind" delivery systems that lack the capability to dynamically track upstream H_2S-mediated regulation and its downstream redox consequences in situ. Recent advances in analytical technologies have enabled partial progress in monitoring cuproptosis-related processes. Surface-enhanced Raman spectroscopy (SERS),[17] which offers molecular fingerprinting capability and single-molecule sensitivity, has emerged as a powerful tool for probing intracellular redox chemistry. Tian and coworkers developed SERS probes to monitor $CuCl_2$-stimulated cuproptosis via the interconversion between Cu^+ and Cu^{2+} in mitochondria.[18]

Received: January 17, 2026
Revised: March 11, 2026
Accepted: March 12, 2026
Published: March 17, 2026

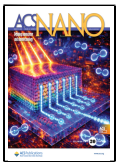

https://doi.org/10.1021/acsnano.6c01009
ACS Nano 2026, 20, 10151−10162

Scheme 1. Schematic Illustration of Cuproptosis Activation Induced by Petal-Like Au−Cu_2O Hybrids in Combination with H_2S/Redox-Metabolic Crosstalk Monitoring

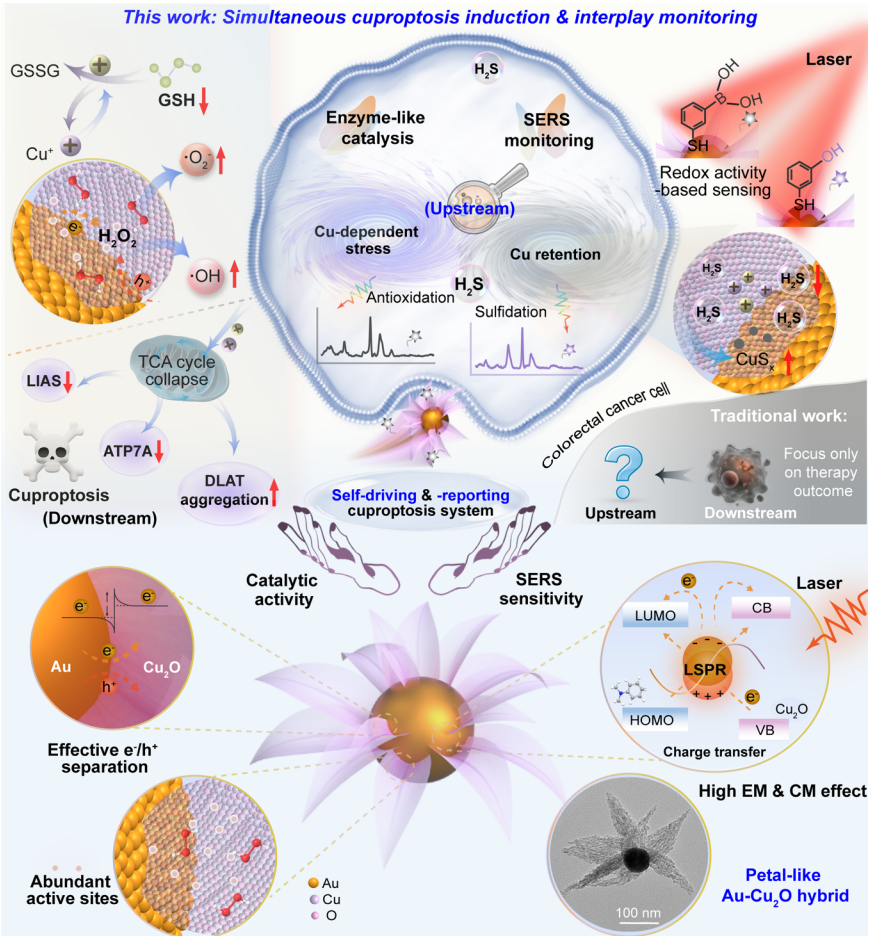

Nevertheless, these probes functioned as passive sensors without built-in cuproptosis-inducing activity, creating a technological gap between induction and monitoring capabilities.

As a promising candidate to combine these capabilities, cuprous oxide (Cu_2O), a semiconductor containing Cu^+ that can generate Cu^{2+} and Cu by disproportionation reactions, have attracted increasing attention thanks to the superior catalytic activities and optical properties.[19−21] In the presence of H_2O_2, Cu_2O can catalyze the generation of •OH while consuming GSH, enhancing the sensitivity of tumor cells to copper-induced cell death.[22] Numerous Cu_2O-based nanomaterials with enzymatic activities and H_2S responsiveness have been developed as therapeutic catalysts for aggravating redox dyshomeostasis. Moreover, Cu_2O could enhance Raman scattering due to the photoinduced electron transfer, but its relatively low enhancement ability impeded the SERS biosensing. Recently, Au−Cu_2O hybrids have been widely explored to greatly enhance catalytic activity originating from a considerable number of copper/oxygen vacancies and possible plasmonic effects.[23] Such hybrid structures are thus promising to facilitate efficient electron transfer at the Au−Cu_2O heterojunction, leveraging the localized electric field for SERS enhancement and sensing.[24]

Despite these advances, the dynamic speciation of copper-sulfide complexes renders cuproptosis analytically elusive, while the mitochondrial localization of key cuproptotic events demands subcellular resolution.[25−27] These issues hindered the monitoring upstream H_2S mediation and downstream effects in a direct way. Activity-based sensing (ABS) strategy leverages chemical probes or enzymatic reactions for real-time monitoring of biological processes via dynamic changes in molecular activity.[28,29] Using this concept, our group have designed several ratiometric SERS sensors to monitor different cell death pathways, such as apoptosis, ferroptosis, by tracking the metabolic changes of downstream biomarkers.[30,31] Accordingly, we hypothesized that combining this SERS-ABS strategy with rationally designed Au−Cu_2O hybrids could enable simultaneous induction and monitoring of cuproptosis processes.

Although the small lattice mismatch between Cu_2O and Au favors the formation of conventional core−shell architectures, such configurations confine the built-in electric field to a narrow interfacial region and often restrict analytes access and efficient redox-coupled charge transfer. In this work, a petal-like Au−Cu_2O hybrid-based theranostic platform has been developed, which enables simultaneous initiation and real-time monitoring of H_2S-mediated cuproptosis in living cells (Scheme 1). Our strategy involves the anisotropic growth of Cu_2O nanoplates on gold nanoparticle surfaces to form a petal-like heterostructure through a surfactant-directed method. Compared to conventional core−shell structures, this petal-like architecture with abundant exposed active sites, promotes effective electron−hole separation, strong electromagnetic and chemical enhancement effect, significantly enhancing both enzyme-like activity and

https://doi.org/10.1021/acsnano.6c01009
ACS Nano 2026, 20, 10151−10162

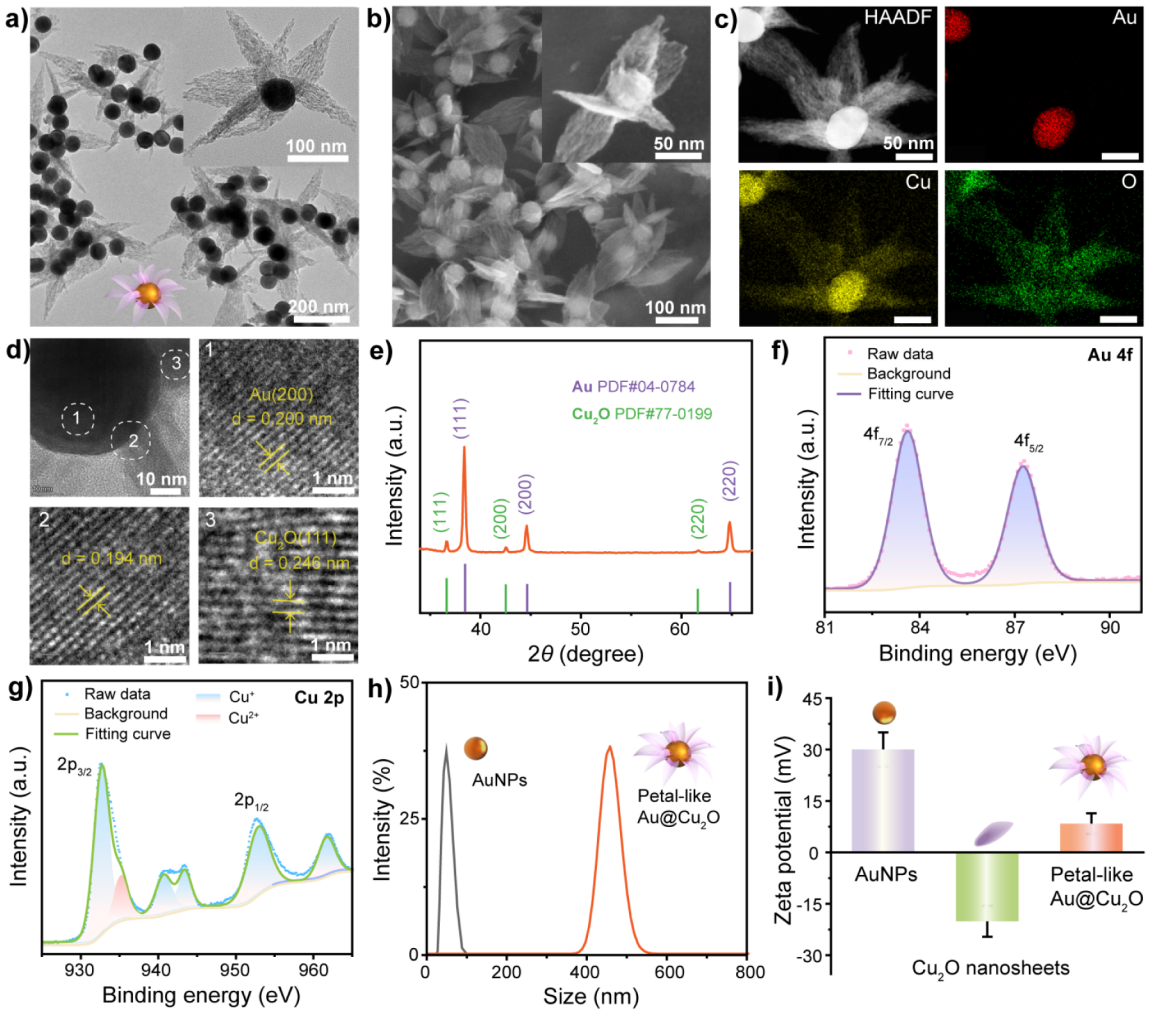

Figure 1. (a) TEM and (b) SEM image of petal-like Au−Cu_2O. (c) HAADF-STEM image and elemental mapping of petal-like Au−Cu_2O. (d) HRTEM image and lattice fringe in the circle regions of 1, 2, and 3. (e) XRD pattern of petal-like Au−Cu_2O. XPS spectra of (f) Au 4f and (g) Cu 2p spectrum. (h) Hydrodynamic size distribution of AuNPs and petal-like Au−Cu_2O. (i) Zeta potential measurement of AuNPs, Cu_2O nanosheets and petal-like Au−Cu_2O.

SERS sensitivity. By leveraging the H_2S-responsive sulfidation behavior, the platform achieves sustained Cu ion release and glutathione depletion while maintaining stable SERS signal output for dynamic detection. Furthermore, using the SERS-ABS strategy, we directly correlate elevated H_2S levels with intracellular copper retention and key downstream cuproptosis events in colorectal cancer models. This dual-functional platform is promising for deciphering the metabolic dynamics of metal ion-mediated cell death and for developing precision theranostic strategies targeting H_2S-altered malignancies.

RESULTS AND DISCUSSION

Synthesis and Characterization of Petal-Like Au−Cu_2O Nanocomposites

Petal-like Au−Cu_2O nanocomposites were synthesized via a surfactant-directed strategy using 50 nm CTAC-stabilized AuNPs as seeds (Figure S1). In this process, sodium dodecyl sulfate (SDS) micelles acted as soft templates, complexing with Cu^{2+} ions and adsorbing onto the AuNP surface. Subsequent reduction of Cu^{2+} by hydrazine hydrate within this confined environment led to the heterogeneous nucleation of Cu_2O on the Au substrate.[32,33] With the reaction time going by, the growth of Cu_2O was extended from the ends to the edges of existing ones (Figure S2), ultimately resulting in the formation of thin Cu_2O nanosheets surrounding AuNPs (Figure 1a). Scanning electron microscopy (SEM) images (Figures 1b and S3) vividly displayed the unique morphology where petal-like Cu_2O nanosheets were anchored onto AuNPs. High-angle annular dark-field scanning TEM (HAADF-STEM) and elemental mapping verified the structure, showing a central Au core with Cu and O distributed throughout the petals (Figure 1c).

Different with previous works in which the lattice spaces between Au and Cu_2O are small, lattice fringes of 0.246 and 0.200 nm, respectively corresponding to the plane of Cu_2O and the {200} plane of Au could be observed (Figure 1d). Despite the lattice mismatch, the Au−Cu_2O interface with a lattice spacing (0.194 nm) was well identified, indicating the formation of the heterojunction probably due to a localized epitaxial growth facilitated by the flexible CTAC/SDS surfactant bilayer at the Au surface.[34] X-ray diffraction (XRD) patterns (Figures 1e and S4) matched well with the standard patterns for Au and Cu_2O, with characteristic peaks for both phases present. The unique petal morphology is attributed to anisotropic growth directed by SDS, which preferentially adsorbs onto the {110}

https://doi.org/10.1021/acsnano.6c01009
ACS Nano 2026, 20, 10151−10162

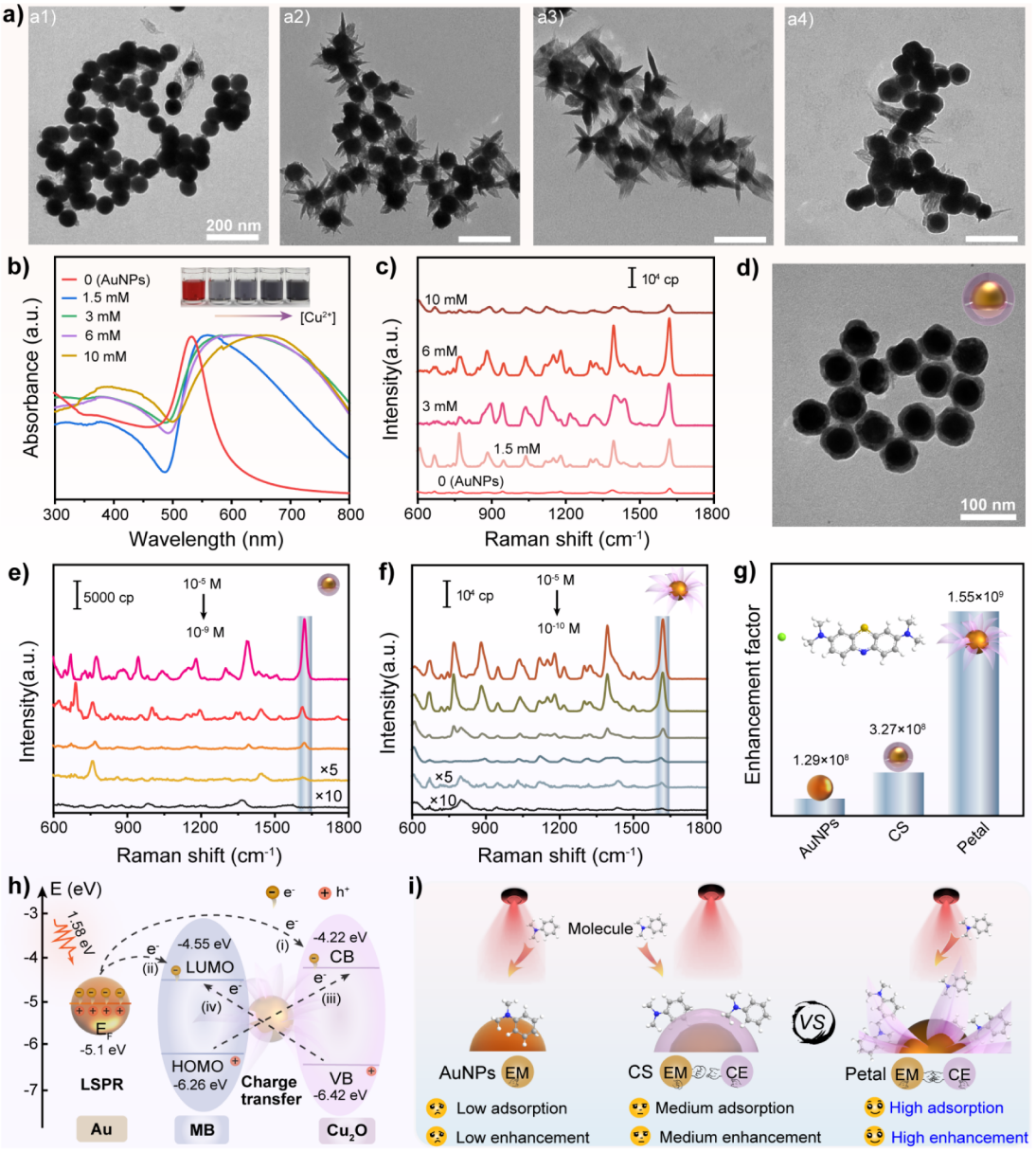

Figure 2. (a) TEM images of Au−Cu_2O hybrids synthesized with increasing Cu^{2+} concentrations (1.5, 3, 6, and 10 mM). (b) UV−vis spectra and corresponding photographs (inset) of the colloidal solutions from (a). (c) SERS spectra of 10^{-5} M methylene blue (MB) obtained from the hybrids in (a) and bare AuNPs. (d) TEM image of the CS structure synthesized for comparison. Concentration-dependent SERS spectra of MB using (e) the CS and (f) the Petal nanostructures. (g) Calculated enhancement factors for AuNPs, CS, and Petal substrates. (h) Charge-transfer diagram of Au, Cu_2O and MB. (i) Comparison of SERS enhancement mechanisms for AuNPs, CS, and Petal hybrids.

facets of Cu_2O, thereby promoting 2D extension along the {111} directions.[33] Electrostatic repulsion between the negatively charged, SDS-capped nanosheets forced them to splay outward from the AuNP surface. In contrast, synthesis without SDS resulted in uneven core−shell clusters (Figure S5), highlighting the essential role of SDS in forming the superstructure. The synthesis was also temperature-sensitive, with optimal structures forming at 30 °C, whereas shorter and sparser petals occurred at 0 °C, mainly due to the high solution viscosity and restricted ion diffusion, limiting the lateral extension of nanosheets (Figure S6a). By contrast, at 80 °C, the increased fluidity and decreased stability of SDS micelles likely led to coarse, loose structures that detach easily (Figure S6b).[32]

X-ray photoelectron spectroscopy (XPS) analysis further validated the chemical states (Figure S7). The Au 4f spectrum in Figure 1f showed doublets at binding energies of 83.6 eV ($4f_{7/2}$) and 87.7 eV ($4f_{5/2}$), characteristic of metallic Au^0. Meanwhile, the Cu 2p spectrum exhibited peaks at 932.7 eV ($2p_{3/2}$) and 952.5 eV ($2p_{1/2}$) (Figure 1g), confirming Cu^+ as the predominant state, with a minor amount of Cu^{2+}. Figure 1h indicates that the hydrodynamic diameter increased to ~450 nm for the petal-like Au−Cu_2O composites, favoring their passive cells targeting and accumulation through enhanced permeability and retention (EPR) effect.[35] Zeta potential measurements showed a significant decrease from +30 mV (AuNPs) to +8 mV (Au−Cu_2O), while pure Cu_2O nanosheets were negatively charged (−22 mV) (Figure 1i and S8). This substantial reduction in positive potential strongly evidenced the successful electrostatic assembly between AuNPs and Cu_2O.

https://doi.org/10.1021/acsnano.6c01009
ACS Nano 2026, 20, 10151−10162

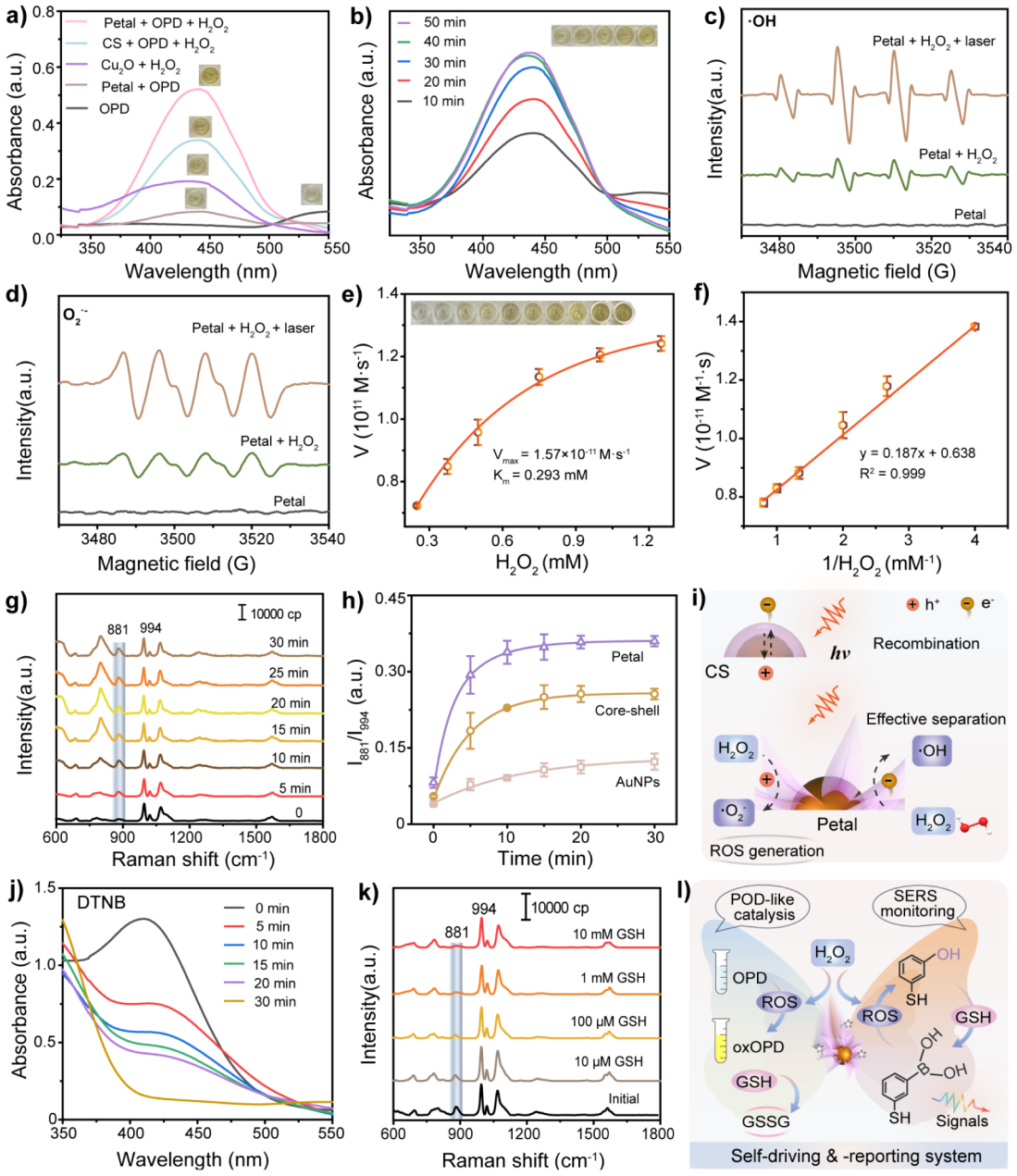

Figure 3. (a) Evaluation of POD-mimic activity via the catalytic oxidation of OPD, showing absorbance of the product (oxOPD) at 437 nm for different reaction conditions. (b) Time-dependent UV−vis spectra of Petal + OPD + H_2O_2 reaction system. (c−d) ESR spectra using DMPO as spin trap, confirming the generation of •OH and $•O_2^-$, respectively, under different conditions including laser irradiation. Steady-state kinetic analysis of the Petal nanozyme: (e) Michaelis−Menten and (f) Lineweaver−Burk plots with H_2O_2 as the substrate. (g) Time-dependent SERS spectra of 3-MPBA (100 μM) reacting with H_2O_2 (100 μM) upon Petal. (h) SERS-based monitoring of H_2O_2 reaction kinetics catalyzed by AuNPs, CS and Petal. (i) Comparison of Plasma-enhanced catalysis for CS and Petal hybrids. (j) Time-dependent GSH depleting ability of petal. (k) SERS spectra of 3-MPBA (100 μM) reacting with fixed H_2O_2 concentration (100 μM) and increasing GSH levels (10 μM−10 mM). (l) Schematic illustration of self-driving and reporting system.

Synergistic SERS Enhancement and Photo-Enhanced Catalytic Activity

The Cu_2O growth was tuned by varying the initial Cu^{2+} concentration (1.5 to 10 mM). The morphology evolved from sparse petals to a well-defined structure at 6 mM, and finally to a continuous shell at 10 mM (Figure 2a). This progression was mirrored in the UV−vis spectra, which showed a progressive red-shift of the Au SPR peak at ∼533 nm (Figure 2b). SERS measurements using the characteristic peak of methylene blue at 1617 cm^{-1} indicated an approximately 6-, 10-, 15- and 2-fold increase respectively compared to the bare AuNPs (Figures 2c and S9). This is likely because at lower concentrations, the initial, sparse growth of Cu_2O petals provided limited surface area and electromagnetic hotspots at the nascent Au−Cu_2O interfaces, resulting in modest SERS enhancement over bare AuNPs. Comparatively, a well-defined petal-like structure observed at 6 mM, maximized the density of intense electromagnetic hotspots within the nanogaps between the Au core and the surrounding petals while simultaneously providing a large surface area for efficient analyte adsorption. However, when Cu^{2+} concentration reached to 10 mM, the overgrowth

https://doi.org/10.1021/acsnano.6c01009
ACS Nano 2026, 20, 10151−10162

and loss of the intricate petal morphology increased the distance between the molecules and the plasmonic Au core, diminishing the SERS activity.

To further validate the superiority of the petal morphology (Petal), its SERS performance was compared to a conventional core−shell (CS) structure. As shown in Figures 2d and S10, using CTAC as the surface ligand under the same 6 mM Cu^{2+} concentration, the Au core was completely coated by Cu_2O shell with a thickness of about 10 nm, consistent with the previous work.[20] Using MB as the model molecule, the Petal enhanced the SERS signal by ∼4-fold compared to the CS (Figure S11). The enhancement performance was further evaluated by the limit of detection (LOD), which was measured to be 10^{-10} M for the Petal, 2 orders of magnitude lower than that of the CS and bare AuNPs (10^{-8} M) (Figures 2e,f and S12). The remarkable enhancement factor (EF) of 1.55×10^9 for the petal-like structure, significantly exceeding those of the core−shell (3.27×10^8) and pure AuNPs (1.29×10^8) (Figure 2g, Tables S1 and S2), underscored a complex enhancement mechanism rather than pure electromagnetic effects. While the finite-difference time-domain (FDTD) simulations limited by pure physical models displayed the CS structure having the lowest field enhancement (Figure S13), its experimentally measured EF was still higher than that of pure AuNPs. This contradiction could be explained by the crucial role of chemical enhancement (CE) of Cu_2O (Figure S14), which possessed intrinsic semiconductor-enhanced Raman scattering capability, even in the CS structure. However, unlike the CS analogue where a continuous Cu_2O shell blocked molecular access to the underlying Au surface, the Petal preserved accessible electromagnetic hotspots while providing a vastly larger Cu_2O surface area for efficient CE. This synergistic mechanism was definitively confirmed using 4-mercaptobenzoic acid (4-MBA), a molecule that bonded strongly onto Au via its thiol group. The resulting SERS intensity (Petal > AuNPs > CS, Figure S15) indicated the presence of exposed Au regions on the Petal, enabling strong chemisorption and electromagnetic enhancement, unavailable in the CS.

Therefore, the interface-rich petal-like Au−Cu_2O hybrid enables multiple charge transfer (CT) pathways, as illustrated in Figure 2h: (i) plasmon-induced hot electrons from Au (−5.1 eV) were injected over the Schottky barrier into the conduction band (CB) of Cu_2O (−4.22 eV), (ii) energetic electrons subsequently transferred into the lowest unoccupied molecular orbital (LUMO) level (−4.55 eV) of adsorbed MB molecules, and (iii) a photoassisted transition occurred from the highest occupied molecular orbital (HOMO) level (−6.26 eV) of MB to the Cu_2O CB as well as (iv) from LUMO to the valence band (VB) of Cu_2O (−6.62 eV) through Herzberg−Teller vibronic coupling.[36,37] Collectively, the petal-like architecture maximized the synergistic interplay between the EM from the Au core and the CE from the Cu_2O semiconductor (Figure 2i), while providing abundant adsorption sites, highly desirable for sensitive SERS analysis.

Benefiting from the integration of AuNPs and Cu^+/Cu^{2+} redox couples, we further explored the enzyme activity of the Petal using colorimetric *o*-phenylenediamine (OPD) assay. As shown in Figure 3a, the Petal effectively catalyzed the oxidation of the chromogenic substrate OPD in the presence of H_2O_2 at pH = 5.0, producing a yellow-colored product (oxOPD), while negligible color change was observed without H_2O_2.[38] Similarly, the catalytic activity exhibited a strong dependence on the morphology of Au−Cu_2O nanostructures (Figure S16). The well-defined petal-like structure obtained at 6 mM Cu^{2+} demonstrated the highest peroxidase (POD)-mimic capability. Figures 3b and S17 show the intensity of absorption peak significantly increased within the first 30 min, indicating that a large amount of generated ROS rapidly participated in OPD oxidation. ESR spectroscopy confirmed the generation of both •OH and $\bullet O_2^-$ radicals,[38] with signal intensity dramatically increasing under laser irradiation, establishing the material as an effective photoenhanced Fenton-like catalyst (Figure 3c and d). Steady-state kinetics was investigated in the mixture containing the Petal and H_2O_2 at different concentration to further evaluate the catalytic activity. According to the Lineweaver−Burk plot, a low Michaelis−Menten constant (K_m = 0.293 mM) and a maximal reaction velocity ($V_{max} = 1.57 \times 10^{-11}$ M·s^{-1}) of the Petal could be obtained (Figure 3e and f), indicating its high specificity for H_2O_2 and high POD-like activity.

The catalytic activity of the nanostructures was further investigated by SERS-ABS strategy, via modifying 3-mercaptophenylboronic acid (3-MPBA), a ROS-responsive Raman probe. Using H_2O_2, one of the most abundant ROS molecule as the model, the reaction between 3-MPBA and H_2O_2 generated a phenol, yielding a distinct SERS peak at 881 cm^{-1} arising from C−O stretching vibrations (Figure 3g), while the peak at 994 cm^{-1} indexed to C−C in-plane bending remained constant.[39] The SERS intensity ratio between I_{881} and I_{994} (I_{881}/I_{994}) showed good linearity with the concentrations of H_2O_2 in the range of 1 μM-10 mM (Figure S18). The response time of Petal was estimated to 10 min based on time-dependent SERS intensity ratio (I_{881}/I_{994}) curves (Figure 3h), obviously lower than those of obtained from CS (15 min) and AuNPs (30 min) (Figure S19), indicating that the developed Petal provided a high temporal resolution. Correspondingly, the absorption increased significantly from the Cu_2O nanosheets to the CS and the Petal Au−Cu_2O nanostructures (Figure 3a), showing the Petal could induce the fastest decomposition of H_2O_2 to generate more ROS.

Then we hypothesized that under plasmon excitation, AuNPs harvested light and produced hot electrons and hot holes (Figure 3i). Compared with the bare AuNPs, the hot electrons with sufficient energy can cross the Schottky barrier and inject into the CB of Cu_2O, leaving hot holes at the AuNPs surface. Nevertheless, electron−hole recombination occurs if the hot carriers are not consumed quickly.[24] Because the surface of the AuNPs in CS nanostructures was totally covered by the Cu_2O shell, the hot holes can be hardly consumed, resulting in a lower reaction efficiency. In contrast, the active sites on the Petal nanostructures were exposed. The plasmon-induced hot electrons were captured by H_2O_2, driving its reduction into highly reactive •OH, while the simultaneous oxidation to •OOH (converted to $\bullet O_2^-$ rapidly).[40] Thus, the efficient electron hole separation would facilitate the generation of ROS under laser irradiation, thereby accelerating the oxidation of 3-MPBA and promoting POD-like catalysis. The nanocomposites also demonstrated rapid glutathione (GSH) depletion within 30 min using 5,5′-dithiobis(2-nitrobenzoic acid) (DTNB) as an indicator (Figure 3j). Furthermore, the effect of GSH on the Petal-induced ROS change was studied using 3-MPBA-functionalized Petal with a favorable structure and signal stability (Figure S20), because GSH is one of the most potent natural scavengers of ROS, maintaining the redox balance within the TME. With GSH concentrations increasing to 10 mM, I_{881}/I_{994} decreased by ∼30% compared with that of the initial (Figure

https://doi.org/10.1021/acsnano.6c01009
ACS Nano 2026, 20, 10151−10162

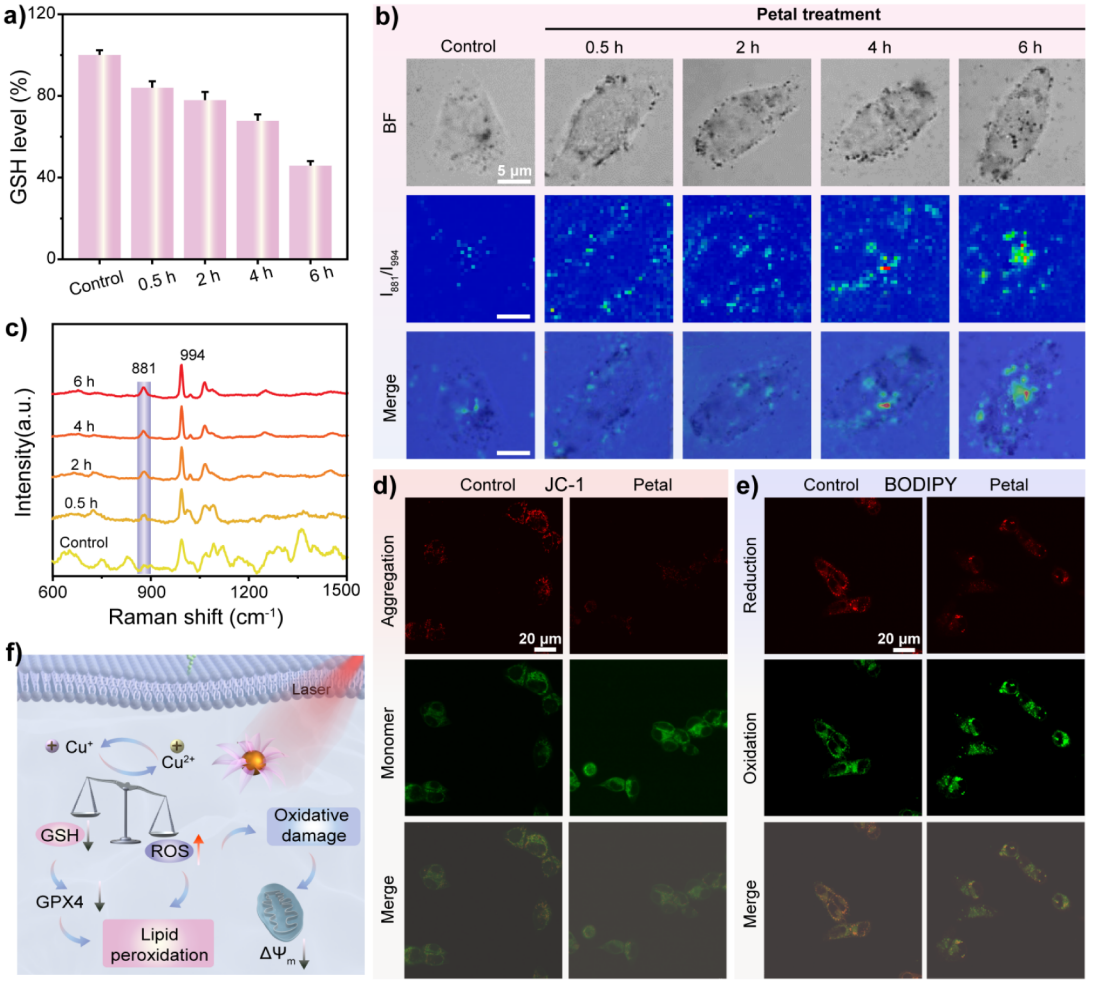

Figure 4. (a) Relative intracellular GSH levels in HCT116 cells after treatment with the Petal hybrid for different durations (0.5, 2, 4, 6 h). Data are mean ± s.d. (n = 3). (b) SERS mapping images of single HCT116 cells based on the I_{881}/I_{994} ratio, after treatment with 3-MPBA-modified Petal for varying times (0.5, 2, 4, and 6 h). Cells treated with 3-MPBA-modified AuNPs for 6 h serve as the control. (c) Representative SERS spectra extracted from the mapping data in (b). (d) JC-1 staining to assess mitochondrial membrane potential (red: J-aggregates, high potential; green: J-monomers, low potential). (e) C11-BODIPY staining to detect lipid peroxidation (red: reduced; green: oxidized). (f) Schematic diagram summarizing the Petal-induced mitochondrial damage and redox dysregulation leading to cell death.

3k), showing that the Petal established an all-in-one platform for self-driving and self-reporting redox modulation (Figure 3l).

Intracellular Redox Disruption and Real-Time SERS Monitoring

Building on the exceptional POD-like activity and self-reporting capability of the petal-like Au−Cu_2O, we first evaluated its cell cytotoxicity and dose-dependent effects. Cytotoxicity assays (CCK-8) revealed that cell viability reduced to ∼40% after 24 h incubation at concentrations ≤50 μg/mL, while exhibiting a concentration and time-dependent decrease (Figure S21). Meanwhile, we discovered that the relative intracellular GSH content showed a time-dependent decrease, dropping to approximately 35% of the initial level after 4 h of treatment (Figure 4a). This sustained GSH consumption created a critical vulnerability in the cellular antioxidant defense system, significantly lowering the threshold for oxidative damage and amplifying the toxicity.[38] SERS mapping based on the I_{881}/I_{994} ratio revealed time-dependent changes in the intracellular oxidative state (Figure 4b). At 0.5 h, the nanocomposites were primarily adsorbed onto the negatively charged cell membrane. With time going by, progressive cellular uptake was observed, accompanied by a steady increase in the intensity of 881 cm^{-1} (Figure 4c). A 9-fold increase of I_{881}/I_{994} could be found when the incubation time reached to 4 h (Figure S22), indicating the capability to simultaneously induce and monitor self-triggered oxidative stress, with the oxidative burden escalating with prolonged incubation.

The catalytic generation of ROS by the internalized Petal nanostructures initiated a cascade of downstream biochemical events indicative of intense cellular stress. JC-1 staining showed a significant increase in green fluorescence (monomeric state) and a decrease in red fluorescence (aggregated state) after 4 h of treatment with the Petal (Figures 4d and S23), indicating a significant loss of mitochondrial membrane potential, a hallmark of mitochondrial dysfunction.[41] Concurrently, the C11-BODIPY probe revealed a substantial increase in lipid peroxidation (Figures 4e and S24), a key event in oxidative cell death pathways.[42] Combined with as-mentioned notable cytotoxicity, the Petal's catalytic activity could be translated into a physiological disruption within the cellular environment (Figure 4f).

H_2S Mediates Copper Retention and Regulates Cuproptosis

H_2S rich in TME of colorectal cancer, can interact with copper, forming CuS_x complexes that may act as a copper reservoir,

https://doi.org/10.1021/acsnano.6c01009
ACS Nano 2026, 20, 10151−10162

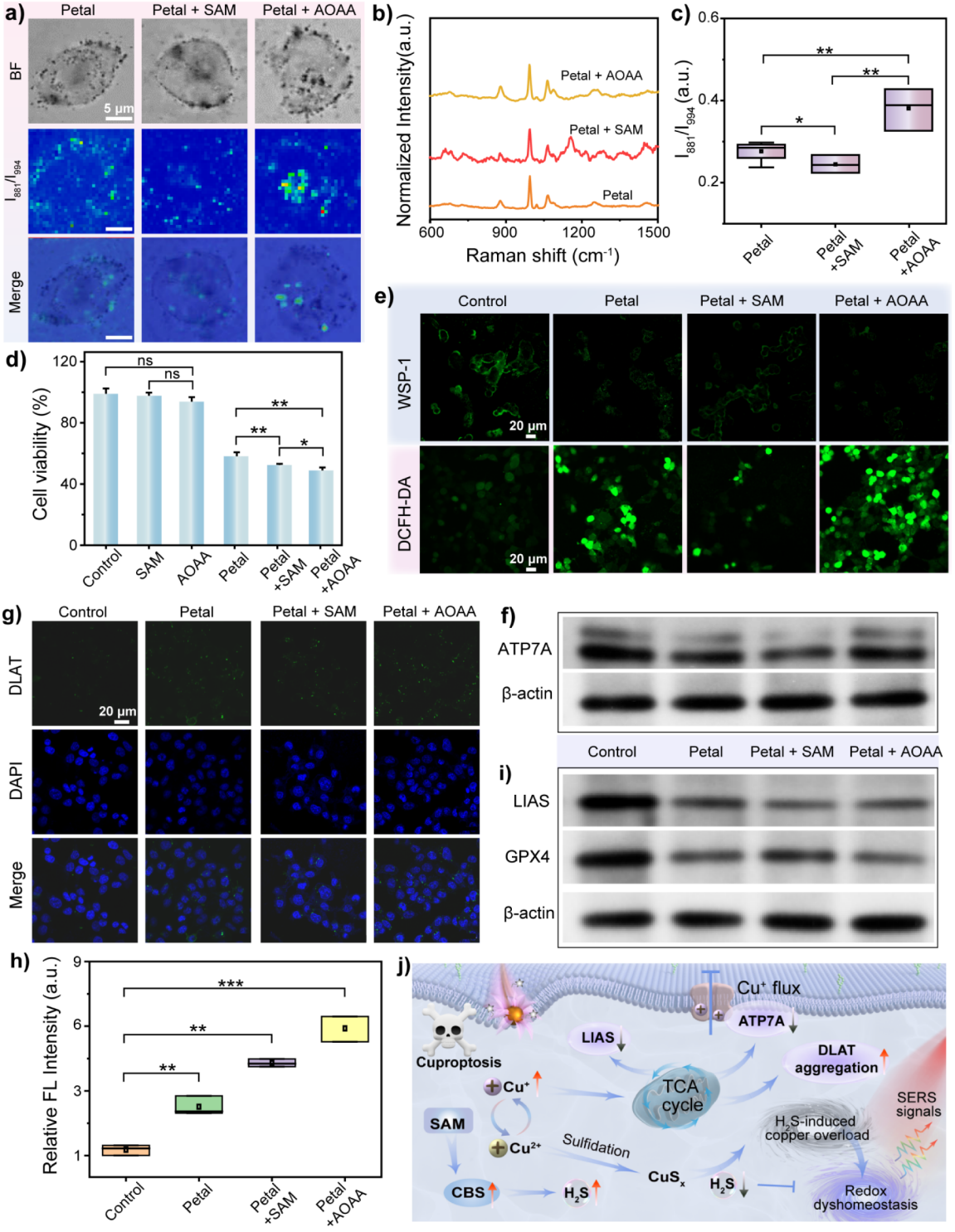

Figure 5. (a) SERS mapping images of single HCT116 cells after pretreatment with the CBS modulator SAM or AOAA, followed by incubation with 3-MPBA-Petal for 2 h. (b) Representative SERS spectra from the mapping data in (a). (c) Quantitative analysis of the I_{881}/I_{994} ratios from (b). Data are mean ± s.d. ($n = 5$). (d) Cell viability assay under different treatment conditions (Control, SAM, AOAA, Petal, Petal + SAM, Petal + AOAA). Data are mean ± s.d. ($n = 5$). (e) Confocal laser fluorescence imaging of intracellular H_2S levels (using WSP-1) and total ROS levels (using DCFH-DA). (f) Western blot analysis of ATP7A protein expression under different treatments. (g) Immunofluorescence staining images showing DLAT expression and oligomerization. (h) Quantitative analysis of the relative fluorescence intensity from (g). (i) Western blot analysis of LIAS and GPX4 protein expression under different treatments. Data are mean ± s.d. ($n = 5$, $^{***}p < 0.001$, $^{**}p < 0.01$, $^{*}p < 0.05$ (Student's two-sided t test). (j) Schematic diagram summarizing the H_2S-mediated alterations in copper retention, distribution, and their impact on cuproptosis-related factors.

potentially modulating copper-dependent cell death (cuproptosis).[14] As shown in Figure S25, exposure to H_2S overnight resulted in a partial shortening and rounding of the nanosheets, but the sulfidation process did not lead to structural collapse, preserving the catalytic activity. The crosstalk of H_2S metabolism and the induction of cuproptosis was further

https://doi.org/10.1021/acsnano.6c01009
ACS Nano 2026, 20, 10151−10162

investigated. S-adenosylmethionine (SAM, a CBS activator[43]) and aminooxyacetic acid (AOAA, a CBS inhibitor[44]) were used to perturb intracellular H_2S levels. SERS results revealed that SAM pretreatment partially relieved oxidative stress with a lower I_{881}/I_{994} ratio, while AOAA pretreatment produced an obviously higher ratio compared to Petal-only treatment (Figure 5a–c). The observed differential oxidative states under SAM and AOAA pretreatment can be attributed to the dual role of H_2S in redox regulation.[15] H_2S as an immediate antioxidant that buffered the oxidative burst (Figure S26), while simultaneously establishing a labile copper reservoir.[4] AOAA-mediated inhibition of H_2S synthesis disturbed the intrinsic antioxidant system. Furthermore, the loss of H_2S-mediated copper sulfidation likely increased the amount of free Cu^+ ions, thereby exacerbating ROS generation.

As evidenced by the results of inductively coupled plasma mass spectrometry (ICP-MS) (Figure S27), SAM treatment promoted substantial copper retention, increasing intracellular copper levels by approximately 1.5-fold compared to the Petal alone, while AOAA treatment attenuated this accumulation. Cell viability assessment revealed SAM or AOAA alone showed minimal cytotoxicity, while the Petal + SAM and Petal + AOAA groups reduced the viability to ~50% (Figure 5d). Furthermore, the cell viability after the treatment of 3-MPBA only remains above 94% after different time (4, 8, 12, 24, 48 h) incubation, indicating its excellent biocompatibility (Figure S28). H_2S levels critically modulated the copper-induced redox changes, consistent with parallel fluorescence assays for H_2S and ROS. As depicted in Figure 5e and Figure S29, compared to the control group, treatment with SAM alone resulted in a more intense green fluorescence signal, while treatment with AOAA alone led to markedly weaker fluorescence. Notably, both the control and the Petal + SAM groups exhibited conspicuous green fluorescence, whereas the Petal + AOAA group displayed substantially diminished fluorescence, confirming that SAM effectively elevates H_2S levels, AOAA suppresses them, and copper ions released from the Petal nanocomposite efficiently sequester H_2S.[45,46] In comparison to the control group, Petal, Petal + SAM, and Petal + AOAA treatments effectively increased the level of total ROS probed by the fluorescence of 2,7-dichlorodihydrofluorescein diacetate (DCFH-DA).

We next examined key protein regulators of copper-induced death. Western blot analysis showed that the nanozyme alone significantly suppressed the expression of ATP7A, a copper efflux pump (Figure 5f). This suppression was more pronounced with SAM cotreatment, likely due to copper-sulfide complex retention creating a feedback inhibition. AOAA pretreatment, by reducing H_2S and thus complex formation, allowed for a partial recovery of ATP7A (Figures 5f and S30).[14] A critical finding emerged from analyzing DLAT, a protein that oligomerizes during cuproptosis. Immunofluorescence revealed that SAM pretreatment, despite yielding lower immediate ROS, strongly enhanced DLAT oligomerization (Figure 5g and h). This suggests that the H_2S-generated copper-sulfide complexes act as a sustained copper source, efficiently delivering copper to its lipoylated protein targets in the mitochondria. In contrast, AOAA-mediated H_2S inhibition led to a surge of highly reactive free copper ions, causing more extensive DLAT aggregation.[46]

In addition, it was found that Petal could destabilize lipoyl synthase (LIAS), a key cuproptosis regulator. Distinct from all other known cell death mechanisms (such as apoptosis, pyroptosis, and ferroptosis), cuproptosis is characterized by the direct binding of intracellular Cu ions to lipoylated enzymes in the tricarboxylic acid (TCA) cycle, resulting in mitochondrial proteotoxicity and Fe–S cluster protein destabilization. As shown, AOAA treatment potently downregulated LIAS expression for cuproptosis amplification (Figures 5i and S31), simultaneously impairing lipoic acid synthesis and copper efflux pathway.[7] Notably, the GPX4 inactivation in Petal-treated cells indicated synergistic activation of ferroptosis pathways, consistent with the observed lipid peroxidation accumulation (Figures 4e and 5i). GPX4 is a central negative regulator of ferroptosis. This synergistic interaction explains the concurrent activation of both cell death pathways observed in our study, with SAM-mediated H_2S elevation partially restoring GPX4 expression by maintaining radical scavenging activity while paradoxically promoting copper retention for cuproptosis execution (Figures 5i and S32).[47,48] Taken together, the petal-like Au–Cu_2O nanocomposite as an efficient copper-delivery platform not only initiating cuproptosis through specific dependence on H_2S mediation, but enabling in situ tracking via SERS monitoring (Figure 5j). It establishes a self-feedback system for precise copper-dependent cell death regulation, promising for theranostic integration in cancer therapy.

CONCLUSIONS

In summary, we have developed a multifunctional petal-like Au–Cu_2O hybrid that combines catalytic therapy and real-time SERS monitoring within a single platform. Its interface-rich structure provided abundant electromagnetic "hotspots" for highly sensitive SERS detection, while also exposing numerous active sites for catalytic reactions. Specifically, the nanocomposite exhibited strong photoenhanced peroxidase-like activity, efficiently generating reactive oxygen species and depleting glutathione to disrupt cellular redox balance. Furthermore, this platform allowed real-time tracking of self-triggered oxidative stress, bridging the gap between induction and observation of biological processes. More importantly, using this system, we elucidated the critical role of H_2S in regulating cuproptosis in colorectal cancer cells. The endogenous H_2S acted as a key modulator of copper-dependent cell death by forming copper-sulfide complexes that controlled copper retention and delivery. This work thus establishes a self-feedback theranostic platform, offering a powerful tool for redox biology research and for developing intelligent and self-reporting anticancer agents.

METHODS

Synthesis of Petal-Like Au–Cu_2O

The 50 nm AuNPs (3 mL) were centrifuged twice at 6000 rpm for 10 min. The precipitate was then redispersed in 200 μL of a mixed solution containing SDS (125 mM) and $Cu(NO_3)_2{\cdot}3H_2O$ (6 mM). Subsequently, the NaOH (50 μL, 2 M) solution was added, and the resulting mixture was allowed to react at 30 °C for 20 min. After that, the $N_2H_4{\cdot}H_2O$ solution (50 μL, 0.374 M) was introduced, and the reaction was continued at 30 °C for 40 min to obtain the final petal-like Au–Cu_2O, and the product was collected via centrifugation at 4500 rpm twice and redispersed in water for further use.

Measurements of Peroxidase-Like Activity of Petal-Like Au–Cu_2O

The peroxidase-like activity of the petal-like Au–Cu_2O nanocomposites was evaluated using a classical chromogenic system with OPD as the substrate. In a typical procedure, 10 μL of OPD (5 mM), 10 μL of H_2O_2 (5, 7.5, 10, 15, 20, and 25 mM), and 20 μL of the petal-like Au–Cu_2O nanocomposites (0.1 mg/mL) were added to B-R buffer (pH = 5.0), and the total reaction volume was adjusted to 200 μL. After

https://doi.org/10.1021/acsnano.6c01009
ACS Nano 2026, 20, 10151–10162

incubation at 37 °C 30 min, the absorbance at 440 nm (corresponding to the oxidized OPD product) was measured by UV−vis spectroscopy.

For each H_2O_2 concentration, the initial reaction rate (V_0) was determined based on the change in absorbance at 440 nm using the Beer−Lambert law, with a molar extinction coefficient (ε) of 17200 $M^{-1}\cdot cm^{-1}$ for oxidized OPD ($A = \varepsilon bc$). The kinetic parameters, Michaelis−Menten constant (K_m) and maximum reaction rate (V_{max}), were derived from the initial rates (V_0) measured at varying substrate concentrations ([S]) using Lineweaver−Burk plot analysis.

$$\frac{1}{V_0} = \frac{K_m + [S]}{V_{max}[S]} = \frac{K_m}{V_{max}}\frac{1}{[S]} + \frac{1}{V_{max}}$$

Intracellular SERS Imaging

The petal-like Au−Cu_2O nanocomposites were first functionalized with 3-MPBA probes, collected by centrifugation, and diluted in complete culture medium prior to use. HCT116 cells were seeded into confocal dishes and cultured overnight. After stimulation with AOAA and SAM, the functionalized nanocomposites were added and incubated with the cells. Before SERS testing, the cells were washed twice with PBS, and then subjected to measurement. Spectral mapping was performed over a defined area of 30 μm × 30 μm with a step size of 1 μm in both the x and y directions.

■ ASSOCIATED CONTENT

Supporting Information

The Supporting Information is available free of charge at https://pubs.acs.org/doi/10.1021/acsnano.6c01009.

The experimental details and characterization of the petal-like and core−shell Au−Cu_2O nanocomposites, the optimization of morphology, the calculation of SERS enhancement factor, catalytic activity tests, the cytotoxicity evaluation, Western blot analysis, and statistical data on H_2S-mediated copper retention and cuproptosis regulation (PDF)

■ AUTHOR INFORMATION

Corresponding Author

Youju Huang − *College of Material, Chemistry and Chemical Engineering, Key Laboratory of Organosilicon Chemistry and Material Technology, Ministry of Education, Hangzhou Normal University, Hangzhou, Zhejiang 311121, P. R. China*; orcid.org/0000-0001-5815-9784; Email: huangyouju@hznu.edu.cn

Authors

Lei Jiang − *College of Material, Chemistry and Chemical Engineering, Key Laboratory of Organosilicon Chemistry and Material Technology, Ministry of Education, Hangzhou Normal University, Hangzhou, Zhejiang 311121, P. R. China*

Qiaoyi Lu − *College of Material, Chemistry and Chemical Engineering, Key Laboratory of Organosilicon Chemistry and Material Technology, Ministry of Education, Hangzhou Normal University, Hangzhou, Zhejiang 311121, P. R. China*

Ermeng Gong − *College of Material, Chemistry and Chemical Engineering, Key Laboratory of Organosilicon Chemistry and Material Technology, Ministry of Education, Hangzhou Normal University, Hangzhou, Zhejiang 311121, P. R. China*

Jiwei Liu − *College of Material, Chemistry and Chemical Engineering, Key Laboratory of Organosilicon Chemistry and Material Technology, Ministry of Education, Hangzhou Normal University, Hangzhou, Zhejiang 311121, P. R. China*

Hongliu Yu − *College of Material, Chemistry and Chemical Engineering, Key Laboratory of Organosilicon Chemistry and Material Technology, Ministry of Education, Hangzhou Normal University, Hangzhou, Zhejiang 311121, P. R. China*

Boyu Ren − *College of Material, Chemistry and Chemical Engineering, Key Laboratory of Organosilicon Chemistry and Material Technology, Ministry of Education, Hangzhou Normal University, Hangzhou, Zhejiang 311121, P. R. China*

Lingniu Yang − *College of Material, Chemistry and Chemical Engineering, Key Laboratory of Organosilicon Chemistry and Material Technology, Ministry of Education, Hangzhou Normal University, Hangzhou, Zhejiang 311121, P. R. China*

Siqi He − *College of Material, Chemistry and Chemical Engineering, Key Laboratory of Organosilicon Chemistry and Material Technology, Ministry of Education, Hangzhou Normal University, Hangzhou, Zhejiang 311121, P. R. China*

Complete contact information is available at: https://pubs.acs.org/10.1021/acsnano.6c01009

Author Contributions

All authors have given approval to the final version of the manuscript. Y.J.H. conceived the concepts and designed the research. E.M.G. and J.W.L. carried out the theoretical analysis. Q.Y.L., H.L.Y., B.Y.R., L.N.Y., and S.Q.H. performed the experiments and contributed to the measurement. L.J., Q.Y.L., and Y.J.H. performed the data analysis and figure development and wrote the paper. All authors discussed the results and commented on the manuscript. L.J. and Q.L. contributed equally to this work.

Notes

The authors declare no competing financial interest.

■ ACKNOWLEDGMENTS

This work was financially supported by the National Natural Science Foundation of China (Grant Nos. U25A20385, 22304042, and 52473209), and the "Pioneer" and "Leading Goose" R&D Program of Zhejiang (2025C02250 (SD2) and 2024C03228).

■ REFERENCES

(1) Tsvetkov, P.; Coy, S.; Petrova, B.; Dreishpoon, M.; Verma, A.; Abdusamad, M.; Rossen, J.; Joesch-Cohen, L.; Humeidi, R.; Spangler, R. D.; Eaton, J. K.; Frenkel, E.; Kocak, M.; Corsello, S. M.; Lutsenko, S.; Kanarek, N.; Santagata, S.; Golub, T. R. Copper Induces Cell Death by Targeting Lipoylated TCA Cycle Proteins. *Science* **2022**, *375*, 1254−1261.

(2) Guo, B.; Yang, F.; Zhang, L.; Zhao, Q.; Wang, W.; Yin, L.; Chen, D.; Wang, M.; Han, S.; Xiao, H.; et al. Cuproptosis Induced by ROS Responsive Nanoparticles with Elesclomol and Copper Combined with α-PD-L1 for Enhanced Cancer Immunotherapy. *Adv. Mater.* **2023**, *35*, 2212267.

(3) Hu, Z.; Shan, J.; Jin, X.; Sun, W.; Cheng, L.; Chen, X. L.; Wang, X. Nanoarchitectonics of in Situ Antibiotic-Releasing Acicular Nanozymes for Targeting and Inducing Cuproptosis-like Death to Eliminate Drug-Resistant Bacteria. *ACS Nano* **2024**, *18*, 24327−24349.

(4) Zhao, F.; Liang, L.; Wang, H.; Wang, C.; Su, D.; Ying, Y.; Li, W.; Li, J.; Zheng, J.; Qiao, L.; et al. H_2S-Activated Ion-Interference Therapy: A Novel Tumor Targeted Therapy Based on Copper-Overload-Mediated Cuproptosis and Pyroptosis. *Adv. Funct. Mater.* **2023**, *33*, 2300941.

(5) Wang, Y.; Yao, X.; Lu, Y.; Ruan, J.; Yang, Z.; Wang, C.; Yang, N.; Gao, Y.; Shi, S. A PROTAC-Based Cuproptosis Sensitizer in Lung Cancer Therapy. *Adv. Mater.* **2025**, *37*, 2501435.

(6) Bao, J.; Wang, J.; Chen, S.; Liu, S.; Wang, Z.; Zhang, W.; Zhao, C.; Sha, Y.; Yang, X.; Li, Y.; Zhong, Y.; Bai, F. Coordination Self-Assembled AuTPyP-Cu Metal-Organic Framework Nanosheets with pH/Ultra-

sound Dual-Responsiveness for Synergistically Triggering Cuproptosis-Augmented Chemotherapy. *ACS Nano* **2024**, *18*, 9100−9113.
(7) Lu, S.; Li, Y.; Yu, Y. Glutathione-Scavenging Celastrol-Cu Nanoparticles Induce Self-Amplified Cuproptosis for Augmented Cancer Immunotherapy. *Adv. Mater.* **2024**, *36*, 2404971.
(8) Chen, L.; Ding, C.; Chai, K.; Yang, B.; Chen, W.; Zeng, J.; Xu, W.; Huang, Y. Nanohole-Array Induced Metallic Molybdenum Selenide Nanozyme for Photoenhanced Tumor-Specific Therapy. *ACS Nano* **2023**, *17*, 18148−18163.
(9) Wu, L.; Lin, H.; Cao, X.; Tong, Q.; Yang, F.; Miao, Y.; Ye, D.; Fan, Q. Bioorthogonal Cu Single-Atom Nanozyme for Synergistic Nanocatalytic Therapy, Photothermal Therapy, Cuproptosis and Immunotherapy. *Angew. Chem., Int. Ed.* **2024**, *63*, No. e202405937.
(10) Lin, H.; Yu, Y.; Zhu, L.; Lai, N.; Zhang, L.; Guo, Y.; Lin, X.; Yang, D.; Ren, N.; Zhu, Z.; Dong, Q. Implications of Hydrogen Sulfide in Colorectal Cancer: Mechanistic Insights and Diagnostic and Therapeutic Strategies. *Redox Biol.* **2023**, *59*, 102601.
(11) Zheng, H.; Zhang, K.; Piao, J.; Mu, C.; Xie, X.; Cheng, M.; Yue, T.; Sun, J.; Li, B.; Wei, Y.; et al. In Situ Valence-Transited Arsenic Nanosheets for Multi-modal Therapy of Colorectal Cancer. *Nat. Commun.* **2025**, *16*, 2088.
(12) Cao, X.; Ding, L.; Xie, Z. Z.; Yang, Y.; Whiteman, M.; Moore, P. K.; Bian, J. S. A Review of Hydrogen Sulfide Synthesis, Metabolism, and Measurement: Is Modulation of Hydrogen Sulfide a Novel Therapeutic for Cancer? *Antioxid. Redox Signal.* **2019**, *31*, 1−38.
(13) Li, X.; Zhang, X.; Song, L.; Li, Y.; Liu, A.; Li, L.; Nešić, M. D.; Li, D.; Peng, L.; Wang, C.; Lin, Q. Nanozyme as Tumor Energy Homeostasis Disruptor to Augment Cascade Catalytic Therapy. *ACS Nano* **2024**, *18*, 34656−34670.
(14) Zhang, W.; Wang, M.; Liu, B.; Chen, H.; Tan, J.; Meng, Q.; Li, J.; Ding, B.; Ma, P.; Lin, J. Glutathione Induced in situ Synthesis of Cu Single-Atom Nanozymes with Anaerobic Glycolysis Metabolism Interference for Boosting Cuproptosis. *Angew. Chem., Int. Ed.* **2024**, *63*, No. e202402397.
(15) Wang, R.; Gu, X.; Li, Q.; Gao, J.; Shi, B.; Xu, G.; Zhu, T.; Tian, H.; Zhao, C. Aggregation Enhanced Responsiveness of Rationally Designed Probes to Hydrogen Sulfide for Targeted Cancer Imaging. *J. Am. Chem. Soc.* **2020**, *142*, 15084−15090.
(16) Dong, S.; Cao, H.; Yuan, Y.; Liang, S.; Fu, Z.; Shi, W.; Xu, Q.; Zhao, X.; Shi, J.; Guo, X.; et al. A Novel "Three-in-One" Copper-Based Metal-Organic Framework Nanozyme Eradicates Colorectal Cancer and Overcomes Chemoresistance for Tumor Therapy. *Adv. Sci.* **2025**, *12*, 2413422.
(17) Song, L.; Jiang, S.; Huang, L.; Chen, L.; Liu, X.; Gong, E.; Yuan, N.; Jian, S.; Huang, Y. Analyte-Targeted Plasmonic Hotspots on Superlattice Mirror Enable Ultra-Broad-Range SERS Sensing of Acetylcholinesterase. *Angew. Chem., Int. Ed.* **2026**, *65*, No. e21361.
(18) Sibug -Torres, S. M.; Grys, D. -B.; Kang, G.; Niihori, M.; Wyatt, E.; Spiesshofer, N.; Ruane, A.; De Nijs, B.; Baumberg, J. J. In Situ Electrochemical Regeneration of Nanogap Hotspots for Continuously Reusable Ultrathin SERS Sensors. *Nat. Commun.* **2024**, *15*, 2022.
(19) Yu, B.; Liu, P.; He, J.; Li, X.; Sun, X.; Peng, B.; Zhang, J.; Ning, Y. Spatially Engineering the Internal Microstructure of a Single Crystal via Nanoparticle Occlusion. *Angew. Chem., Int. Ed.* **2025**, *64*, No. e202505637.
(20) Zeng, J.; Ding, C.; Chen, L.; Yang, B.; Li, M.; Wang, X.; Su, F.; Liu, C.; Huang, Y. Multienzyme-Mimicking Au@Cu_2O with Complete Antioxidant Capacity for Reactive Oxygen Species Scavenging. *ACS Appl. Mater. Interfaces* **2023**, *15*, 378−390.
(21) Ning, S.; Lyu, M.; Zhu, D.; Lam, J. W. Y.; Huang, Q.; Zhang, T.; Tang, B. Z. Type-I AIE Photosensitizer Loaded Biomimetic System Boosting Cuproptosis to Inhibit Breast Cancer Metastasis and Rechallenge. *ACS Nano* **2023**, *17*, 10206−10217.
(22) Li, Z.; Yang, J.; Ren, B.; Fan, Q.; Huang, L.; Guo, S.; Zhou, R.; Chen, S.; Feng, J.; Yan, C.; et al. Double-Layered Hollow Mesoporous Cuprous Oxide Nanoparticles for Double Drug Sequential Therapy of Tumors. *Adv. Mater.* **2024**, *36*, 2313212.
(23) Ashok Kumar, E.; Jiann Wang, T.; Chang, Y. H. Ultrasensitive SERS Substrates Based on Au Nanoparticles Photo-Decorated on Cu_2O Microspheres for the Detection of Rhodamine B and Methylene Blue. *Appl. Surf. Sci.* **2022**, *585*, 152696.
(24) Jia, H.; Li, F.; Chow, T. H.; Liu, X.; Zhang, H.; Lu, Y.; Wang, J.; Zhang, C. Construction of Spatially Separated Gold Nanocrystal/Cuprous Oxide Architecture for Plasmon-Driven CO_2 Reduction. *Nano Lett.* **2022**, *22*, 7268−7274.
(25) Zhang, H.; Xia, J.; Xie, L.; Hao, M.; Liang, W.; Wang, S.; Dong, X.; Li, Y.; Mu, Q. Mitochondria and Anaerobic Glycolysis-Targeted Self-Assembled Copper Complex Nanoparticles for Boosting Cuproptosis-Immunotherapy. *Adv. Compos Hybrid Mater.* **2025**, *8*, 45.
(26) Wang, S.; Liu, X.; Wei, D.; Zhou, H.; Zhu, J.; Yu, Q.; Luo, L.; Dai, X.; Jiang, Y.; Yu, L.; Yang, Y.; Tan, W. Polyvalent Aptamer Nanodrug Conjugates Enable Efficient Tumor Cuproptosis Therapy through Copper Overload and Glutathione Depletion. *J. Am. Chem. Soc.* **2024**, *146*, 30033−30045.
(27) Xu, W.; Suo, A.; Aldai, A. J. M.; Wang, Y.; Fan, J.; Xia, Y.; Xu, J.; Chen, Z.; Zhao, H.; Zhang, M.; Qian, J. Hollow Calcium/Copper Bimetallic Amplifier for Cuproptosis/Paraptosis/Apoptosis Cancer Therapy via Cascade Reinforcement of Endoplasmic Reticulum Stress and Mitochondrial Dysfunction. *ACS Nano* **2024**, *18*, 30053−30068.
(28) Jiang, Y.; El Khoury, E.; Pezacki, A. T.; Qian, N.; Oi, M.; Torrente, L.; Miller, S. G.; Ralle, M.; DeNicola, G. M.; Min, W.; Chang, C. J. An Activity-Based Sensing Approach to Multiplex Mapping of Labile Copper Pools by Stimulated Raman Scattering. *J. Am. Chem. Soc.* **2024**, *146*, 33324−33337.
(29) Xie, X.; Li, G.; Pezacki, A. T.; Gao, J.; Oi, M.; Chang, C. J. An Alkyne-Directed Cleavage Approach for Activity-Based Cu(I) Sensing Reveals Manganese-Promoted Sensitization of Cuproptosis. *J. Am. Chem. Soc.* **2025**, *147*, 34564−34574.
(30) Jiang, L.; Chen, H. Y.; He, C. H.; Xu, H. B.; Zhou, Z. R.; Wu, M. S.; Fodjo, E. K.; He, Y.; Hafez, M. E.; Qian, R. C.; Li, D. W. Dual-Modal Apoptosis Assay Enabling Dynamic Visualization of ATP and Reactive Oxygen Species in Living Cells. *Anal. Chem.* **2023**, *95*, 3507−3515.
(31) Jiang, L.; Zhao, M.; Xu, H.; Ding, X.; Lu, Q.; Liu, J.; Song, L.; Gong, L.; Li, D.; Huang, Y. Plasmonic Nanoparticle Monolayer-Decorated Nanopipette Enabling in situ Monitoring of Single-Cell Redox Metabolism. *Angew. Chem., Int. Ed.* **2025**, *64*, No. e202502129.
(32) Schäfer, K.; Kolli, H. B.; Killingmoe Christensen, M.; Bore, S. L.; Diezemann, G.; Gauss, J.; Milano, G.; Lund, R.; Cascella, M. Supramolecular Packing Drives Morphological Transitions of Charged Surfactant Micelles. *Angew. Chem., Int. Ed.* **2020**, *59*, 18591−18598.
(33) Jiang, Y.; Xia, T.; Shen, L.; Ma, J.; Ma, H.; Sun, T.; Lv, F.; Zhu, N. Facet-Dependent Cu_2O Electrocatalysis for Wearable Enzyme-Free Smart Sensing. *ACS Catal.* **2021**, *11*, 2949−2955.
(34) Xu, W.; Jia, J.; Wang, T.; Li, C.; He, B.; Zong, J.; Wang, Y.; Fan, H. J.; Xu, H.; Feng, Y.; Chen, H. Continuous Tuning of Au-Cu_2O Janus Nanostructures for Efficient Charge Separation. *Angew. Chem., Int. Ed.* **2020**, *59*, 22246−22251.
(35) Forgham, H.; Chang, Y.; Wang, Y.; Zhu, J.; Liu, L.; Biggs, H.; Kakinen, A.; Jiang, Y.; You, X.; Thurecht, K. J.; et al. The Evolution of Nanomedicine: The Rise of Next-Generation Nanomaterials in Cancer Nanomedicine. *Sci. Adv.* **2025**, *11*, No. eadx1576.
(36) Yao, Y.; Zhao, Y.; Zhang, H.; Pan, W.; Liang, W.; Jiang, Y.; Yan, X.; Yan, Y. Ultrafast Laser-Induced 1T'/2H-$MoTe_2$ Nanopattern with Au-Nanoclusters for Raman Monitoring of Cellular Drug Metabolism. *ACS Nano* **2025**, *19*, 16732−16743.
(37) Xie, Y.; Chen, C.; Zhang, C.; Xu, L.; Li, Z.; Ren, W.; Xu, X.; Ren, Y.; Lin, J.; Wu, A. Synergistic Enhancement of Ultrahigh SERS Activity via Cu_2O@Ag Core-Shell Structure for Accurate Label-Free Identification of Breast Tumor Subtypes. *Nano Today* **2024**, *54*, 102140.
(38) Zhu, W.; Wu, J.; Kang, Y.; Xue, P. $Cu_2O/CuVO_3$ Nano-Heterojunction as a Highly Active Therapeutic Catalyst for Aggravating Redox Dyshomeostasis of Neoplastic Cells. *Adv. Mater.* **2025**, *37*, 2502407.
(39) Wang, F.; Wan, H.; Chen, L.; Qiu, T.; Jiang, L.; Guo, Z.; Chen, F.; Cao, Y. Gemini SERS for Cross-Category Biomarker Detection and Early Warning of Sudden Cardiac Death in Acute Coronary Syndrome. *ACS Nano* **2025**, *19*, 37802−37814.

https://doi.org/10.1021/acsnano.6c01009
ACS Nano 2026, 20, 10151−10162

(40) Zhou, L.; Huang, Q.; Xia, Y. Plasmon-Induced Hot Electrons in Nanostructured Materials: Generation, Collection, and Application to Photochemistry. *Chem. Rev.* **2024**, *124*, 8597−8619.
(41) Liu, N.; Lin, Q.; Huang, Z.; Liu, C.; Qin, J.; Yu, Y.; Chen, W.; Zhang, J.; Jiang, M.; Gao, X.; Huo, S.; Zhu, X. Mitochondria-Targeted Prodrug Nanoassemblies for Efficient Ferroptosis Based Therapy via Devastating Ferroptosis Defense Systems. *ACS Nano* **2024**, *18*, 7945−7958.
(42) Le, X. T.; Nguyen, N. T.; Lee, W. T.; Yang, Y.; Choi, H. -G.; Youn, Y. S. Peroxidase-Mimicking Iron-Based Single-Atom Upconversion Photocatalyst for Enhancing Chemodynamic Therapy. *Adv. Funct. Mater.* **2024**, *34*, 2401893.
(43) Li, Y.; Liu, G.; Cheng, S.; Zhang, J.; Yao, X.; Xie, X.; Xu, C.; Tang, Y.; Wang, X.; Tang, B. Cellular Redox Regulation and Fluorescence Imaging. *Chem. Rev.* **2025**, *125*, 7725−7810.
(44) Wang, D.; Yang, H.; Zhang, Y.; Hu, R.; Hu, D.; Wang, Q.; Liu, Y.; Liu, M.; Meng, Z.; Zhou, W.; et al. Inhibition of Cystathionine *β*-Synthase Promotes Apoptosis and Reduces Cell Proliferation in Chronic Myeloid Leukemia. *Signal Transduct. Target. Ther.* **2021**, *6*, 52.
(45) Dong, C.; Zhu, T.; Sun, J.; Dong, X.; Sun, L.; Gu, X.; Zhao, C. Self-Assembled Activatable Probes to Monitor Interactive Dynamics of Intracellular Nitric Oxide and Hydrogen Sulfide. *Anal. Chem.* **2024**, *96*, 1259−1267.
(46) Huang, L.; Zhu, J.; Wu, G.; Xiong, W.; Feng, J.; Yan, C.; Yang, J.; Li, Z.; Fan, Q.; Ren, B.; Li, Y.; Chen, C.; Yu, X.; Shen, Z. A Strategy of "Adding Fuel to the Flames" Enables a Self-Accelerating Cycle of Ferroptosis-Cuproptosis for Potent Antitumor Therapy. *Biomaterials* **2024**, *311*, 122701.
(47) Liu, H.; Yang, Y.; Zhang, N.; Hou, Y.; Zhang, Z.; Yu, X.; Huang, Y.; Yan, B.; Zhou, H.; Mu, M.; Gao, Y.; Guo, K.; Yang, M.; Sun, X. Overcoming Photothermal Resistance of Gastric Cancer by Bionic 2D Iron-Based Nanoplatforms with Precise CRISPR/Cas9 Delivery. *ACS Nano* **2025**, *19*, 18188−18202.
(48) Hu, J.; Zhu, J.; Wang, K.; Yan, X.; Xu, L.; Zhang, X.; Ding, H.; Yang, P.; Hu, S.; Xie, R. Engineered-Doping Strategy for Self-Sufficient Reactive Oxygen Species Blossom to Amplify Ferroptosis/Cuproptosis Sensibilization in Hepatocellular Carcinoma Treatment. *Adv. Funct. Mater.* **2024**, *34*, 2405383.

https://doi.org/10.1021/acsnano.6c01009
ACS Nano 2026, 20, 10151−10162